Journal of the Korean Ceramic Society (2024) 61:327–334
https://doi.org/10.1007/s43207-023-00361-x

ORIGINAL ARTICLE

Exploring the role of TiN electrodes in the formation of ferroelectric $Hf_xZr_{1-x}O_2$ thin films through transmission electron microscopy

Sojin Kim[1] · Jaewook Lee[2] · Jong Hyeok Seo[3] · Jinseok Hong[1] · Ji-Hwan Kwon[3] · Min Hyuk Park[2] · Seung-Yong Lee[1]

Received: 30 October 2023 / Revised: 8 December 2023 / Accepted: 15 December 2023 / Published online: 23 January 2024
© The Korean Ceramic Society 2024

Abstract
The development of ferroelectric HfO_2-based thin films, with their potential to revolutionize semiconductor technology, relies on comprehending the factors that drive the formation of the polar orthorhombic phase. Although TiN electrodes are known to facilitate orthorhombic phase formation, a comprehensive understanding is still lacking. Our study offers an in-depth exploration of the pivotal role played by TiN electrodes in shaping ferroelectric $(Hf,Zr)O_2$-based thin films using transmission electron microscopy (TEM). Through direct depositions of $Hf_{0.65}Zr_{0.35}O_2$ (HZO) thin films and TiN masks onto a silicon membrane TEM grid, we enable a straightforward structural comparison between HZO thin films annealed with and without a TiN capping layer. This approach ensures uniform conditions across all parameters, except the presence of the TiN capping layer, while eliminating potential artifacts introduced during the TEM sampling. Our comprehensive analysis, incorporating electron diffraction, high-resolution TEM (HR-TEM), and electron energy loss spectroscopy (EELS), delves into the possible influences of factors such as tensile strain, oxygen vacancies, and the surface atomic mobility constraint effect induced by the TiN capping layer. The results underscore the dominant role of TiN in surface atomic mobility constraint, thereby significantly contributing to the formation of ferroelectric HZO. This research promises to advance our understanding of ferroelectric materials, thus expediting the progress of ferroelectric and semiconductor technology.

Keywords Ferroelectricity · Hafnium zirconium oxide · Transmission electron microscopy · Titanium nitride electrode · Thin film

1 Introduction

Recent advancements in ferroelectric materials, particularly within HfO_2-based thin films [1], hold the potential to revolutionize ferroelectric and semiconductor technology, impacting a wide array of applications like non-volatile memory devices, sensors, and actuators [2, 3]. Nevertheless, this promise necessitates an extensive exploration of the fundamental aspects of HfO_2-based thin films. These films can exist in various phases, notably tetragonal ($P4_2/nmc$), monoclinic ($P2_1/c$), and orthorhombic ($Pca2_1$), each distinguished by subtle atomic variations in hafnium and oxygen positions [4–6]. Ferroelectricity in HfO_2-based thin films exclusively arises from the polar orthorhombic phase, underscoring the significance of effectively inducing this phase in these thin films [4]. However, the orthorhombic phase is metastable, making it kinetically driven and susceptible to factors such as dopants [1, 7–9], oxygen vacancy concentration [10–13], film thickness [14–17], cooling rates [18], mechanical stresses [19–21], etc. [22]. Thus, gaining a profound understanding of these factors that facilitate orthorhombic phase formation is of paramount importance.

The choice of electrodes significantly impacts the modification of ferroelectric properties in HfO_2-based thin films, given their influence on the aforementioned factors. In this context, TiN electrodes have garnered increasing attention

Sojin Kim, Jaewook Lee contributed equally to this work.

Min Hyuk Park
minhyuk.park@snu.ac.kr

Seung-Yong Lee
syonglee@hanyang.ac.kr

[1] Division of Materials Science and Engineering, Hanyang University, Seoul, Republic of Korea

[2] Department of Materials Science and Engineering & Inter-University Semiconductor Research Center, Seoul National University, Seoul, Republic of Korea

[3] Korea Research Institute of Standards and Science (KRISS), Daejeon, Republic of Korea

for their potential to enhance the functionality of ferroelectric HfO_2-based thin films during the annealing process [1]. Several studies have hinted at how TiN can induce the orthorhombic phase formation of HfO_2-based thin films by creating oxygen-deficient conditions [13], providing tensile strain [20], and exerting a surface atomic mobility constraint effect, often called as a mechanical confinement effect [1]. However, a comprehensive comparison of these effects has remained a challenge, resulting in a limited overall understanding.

We extensively explore the pivotal role of TiN in shaping ferroelectric $(Hf,Zr)O_2$-based thin films during the annealing process through a novel approach tailored for comprehensive transmission electron microscopy (TEM) investigations. Instead of relying on the traditional TEM sampling method from the fabricated device, we devise a direct approach by depositing $Hf_{0.65}Zr_{0.35}O_2$ (HZO) thin films and TiN masks onto a silicon membrane TEM grid, effectively establishing a metal–ferroelectric–insulator–semiconductor (MFIS) structure on a TEM grid. This method ensures a consistent environment across all parameters, except for the presence of the TiN capping layer in the areas with or without the TiN masks, while simultaneously eliminating potential artifacts that can be introduced during TEM sampling. Notably, this approach facilitates a straightforward structural comparison between HZO thin films annealed with the presence of a TiN top electrode (post-metallization annealing; PMA), or those without the TiN top electrode (post-deposition annealing; PDA). Moreover, this configuration enables plan-view observations, offering a significantly wider field of view compared to conventional sectional-view observations. Utilizing this innovative TEM design, we perform a comprehensive examination of phase distribution, grain size, oxygen vacancies, and tensile stress/strain in HZO thin films under the influence of a TiN capping layer. Our research findings distinctly underscore the inhibitory effect of TiN on grain growth by surface atomic mobility constraint as the dominant factor contributing to the formation of the polar orthorhombic phase in HZO thin films during the annealing process, surpassing other potential influences. This study has the potential to advance our comprehension of ferroelectric materials and, consequently, expedite the development of cutting-edge applications in electronics, data storage, and various other fields.

2 Experimental Section

The 6.3 nm-thick $Hf_{0.65}Zr_{0.35}O_2$ (HZO) thin film was deposited at 270 °C using thermal atomic layer deposition (ALD) on a 5 nm-thick amorphous Si membrane TEM sampling grid. The $Hf[N(CH_3)C_2H_5]_4$ and $Zr[N(CH_3)C_2H_5]_4$ precursors were used to deposit HfO_2 and ZrO_2 layers, respectively, and ozone (200 g/m^3) was used as an oxygen reactant. Subsequently, 6 nm-thick TiN top electrodes (TE) were deposited via radio frequency sputtering and patterned into a circular shape with a diameter of 150 μm using a shadow mask. To crystallize the HZO film, post-metallization annealing (PMA) was carried out at 600 °C for 30 s under a N_2 atmosphere. Since the TiN TE covers only a portion of the HZO film, the regions without TiN TE are assumed to be subjected to post-deposition annealing (PDA).

For the electrical measurement, the HZO film, TiN TE deposition, and annealing with the same fabrication process as in the TEM sampling grid were performed on a highly doped p-type Si substrate (p^+ Si, resistivity < 0.005 Ω·cm). Before film deposition, the native SiO_x layer was etched using a hydrofluoric acid solution. The electric measurements were carried out using a semiconductor parameter analyzer (4200A-SCS, Keithley). The double remanent polarization ($2P_r$) values were extracted from positive up negative down (PUND) measurements where two positive and two negative triangular pulses with a rising/falling/delay time of 250 μs were sequentially applied.

For the TEM measurement, selected area electron diffraction (SAED) patterns were obtained from a JEOL JEM-2010 200 kV TEM instrument with a LaB_6 electron gun. To calculate the lattice parameters from the SAED patterns, we utilized several prominent peaks in the SAED patterns. The peaks used for the lattice parameter calculations of each phase are as follows. For PDA region: (1) monoclinic phase: peaks for {100} at 1.977 nm^{-1}, {011} at 2.758 nm^{-1}, {11–1} at 3.255 nm^{-1}, and {002} at 3.889 nm^{-1}. (2) tetragonal phase: peaks for {101} at 3.475 nm^{-1} and {110} at 3.944 nm^{-1}. (3) orthorhombic phase: peaks for {010} at 1.977 nm^{-1}, {110} at 2.758 nm^{-1}, and {111} at 3.475 nm^{-1}. For PMA region: (1) tetragonal phase: peaks for {101} at 3.558 nm^{-1} and {110} at 4.064 nm^{-1}. (2) orthorhombic phase: peaks for {010} at 2.013 nm^{-1}, {110} at 2.905 nm^{-1}, and {111} at 3.558 nm^{-1}. High-resolution TEM (HR-TEM) images and electron energy loss spectroscopy (EELS) data were acquired at an accelerated voltage of 300 kV from Thermo Scientific Spectra 300, a double Cs-corrected S/TEM instrument with GIF Continuum for EELS measurement.

3 Results and Discussions

3.1 Approach for TEM Investigation of $Hf_{0.65}Zr_{0.35}O_2$ (HZO) Thin Films

Our approach for TEM investigations is illustrated in Fig. 1. We directly deposited a 6.3 nm-thick $Hf_{0.65}Zr_{0.35}O_2$ (HZO) thin film and 6 nm-thick TiN top electrode (TE) masks sequentially onto a 5 nm-thick amorphous silicon

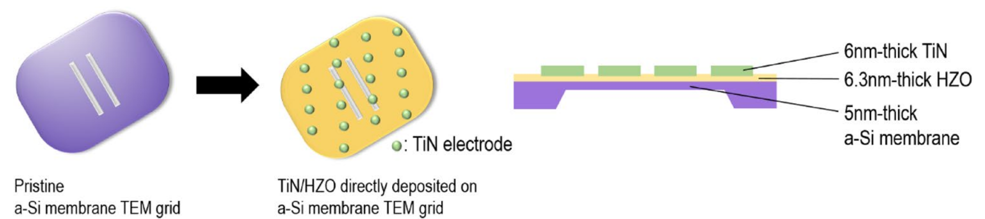

Fig. 1 Schematic illustration of our TEM investigation approach involving the direct deposition of 6 nm-thick TiN masks and a 6.3 nm-thick $Hf_{0.65}Zr_{0.35}O_2$ (HZO) thin film on an amorphous silicon membrane TEM grid

membrane TEM sampling grid, establishing an MFIS structure. We opted for an amorphous silicon membrane, instead of a crystalline silicon membrane, to avoid interference with the HZO thin film from electron diffraction patterns and simplify the indexing of the polymorphic HZO thin film. Subsequent to the deposition of the HZO thin film and TiN TE masks, the grid was subjected to an annealing process at 600 °C for 30 s in an N_2 atmosphere to crystallize the HZO thin film. Since the TiN TE masks with a radius of 150 µm only cover a portion of the HZO thin film, both regions of the HZO thin film, with or without the TiN capping layer, coexist on the same grid. It enables both post-metallization annealing (PMA) and post-deposition annealing (PDA) of the HZO thin film on the same grid, allowing for direct TEM comparisons of both areas within a single specimen. Both areas underwent identical fabrication conditions, except for the presence or absence of the TiN capping layer, making it a reliable means of investigation with the TiN capping layer as the only independent variable. Additionally, this approach eliminates the need for further sampling processes in TEM observations, thereby minimizing potential artifacts and ensuring the reliability of the investigations. Furthermore, this setup enables plan-view observations, providing a significantly broader field of view that allows for the examination of numerous HZO grains without overlap. This addresses a significant limitation of the typical conventional sectional-view TEM observations.

3.2 Ferroelectric Properties of HZO Thin Films

The TiN electrode is recognized as a significant contributor to enhancing the ferroelectric properties of $(Hf,Zr)O_2$-based thin films through several mechanisms. These include inducing tensile strain [20], increasing oxygen vacancy concentration [13], and exerting a surface atomic mobility constraint effect that hinders grain growth and lattice distortion, which is often referred to as a mechanical confinement effect [1]. In line with the established knowledge, the electrical characterization also demonstrates enhanced ferroelectric properties in HZO thin films which were crystallized under the presence of the TiN TE (PMA) compared to those annealed without TiN TE (PDA), as depicted in Fig. 2. Since it is highly challenging to directly obtain a hysteresis loop from an amorphous Si membrane, the HZO films were deposited on a highly doped p-type Si (p^+-Si) substrate as described in the Experimental Section. Figure 2a shows the fabricated MFIS stack where a PUND pulse was applied to the TiN top electrode while the Si substrate was grounded. The J-V and P–V curves extracted from PUND measurements for PMA and PDA samples are shown in Fig. 2b and c, respectively. They were obtained by subtracting non-switching currents under U or D pulses from the switching current under P or N pulses to accurately measure the remanent polarization without the contribution of the leakage current and dielectric responses.

The $2P_r$ value of 23.5 µC/cm^2 observed for the PMA sample was higher than that of the PDA sample (15.9

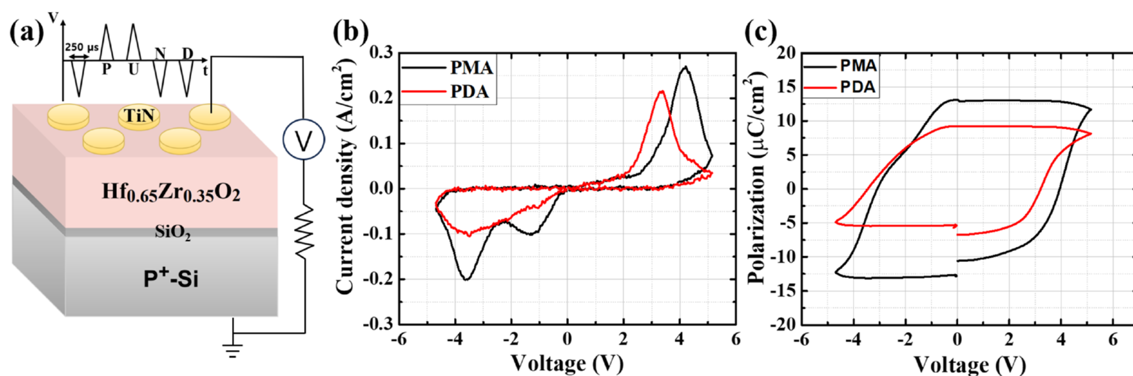

Fig. 2 **a** PUND measurement scheme of fabricated TiN/HZO/p+-Si capacitor with a 6.3 nm-thick HZO film. **b** Current density–voltage (J–V) and **c** polarization-voltage (P–V) curves for PMA and PDA samples obtained from PUND measurements

μC/cm^2) by ~ 48%. It should be noted that the $2P_r$ values estimated from the PUND measurement would be slightly overestimated by imperfect removal of the leakage current due to the ferro-resistive switching, evidenced by the rounded edges of the P–V curves. However, it could be evidenced by the J-V curves in Fig. 2b that the higher $2P_r$ value of PMA samples compared to that of PDA samples did not originate from the difference in the leakage current. Based on the observed higher $2P_r$ value for the PMA sample, it could be postulated that the fraction of the ferroelectric orthorhombic phase might be higher than that in the PDA sample, which will be discussed more thoroughly with the structural analysis in the following sections. The positive (V_{c+}) and negative V_c (V_{c-}) values were ~ +4.0 and ~ −3.0 V for the PMA sample and ~ +3.0 and ~ −3.5 V for the PDA sample as shown in Fig. 2c, which seem rather high considering the 6.3 nm thickness of HZO film, could be attributed to the existence of low-k SiO_2 (k = 3.9) interfacial layer. Considering the generally known k values and thickness of HZO (~ 30 and 6.3 nm) and native SiO_2 interfacial layer (3.9 and 2 nm), the expected V_c value with the accumulation-state Si is ~ 3.2 V. Therefore, the observed V_c values are believed to be reasonable. Compared to the $(V_{c+} + V_{c-})/2$ PDA sample (~ −0.25 V), that of the PMA sample (~ +0.5 V) was higher, suggesting that the Schottky barrier of top TiN/HZO interface in PMA sample would be higher than that of PDA sample with resulting positive shift of the P–V curve possibly due to the higher quality of interface with lower concentration of defects formed during the sputtering of top electrode.

3.3 Phase Distribution in HZO Thin Films

To explore the underlying causes of differences in ferroelectric properties and to determine the crucial impact of the TiN TE during the annealing process, we initially compared the phase distribution using high-resolution TEM (HR-TEM) images and selected area electron diffraction (SAED) patterns (Fig. 3). In Fig. 3a, we compared the proportions of orthorhombic ($Pca2_1$)/tetragonal ($P4_2/nmc$) and monoclinic ($P2_1/c$) phases of HZO thin films in PMA and PDA regions. This determination was made by indexing more than 30 fast Fourier-transformed (FFT) patterns from HR-TEM images in each region. For simplicity, orthorhombic and tetragonal phases were considered together due to their similarity in SAED patterns. Additionally, grains that can be indexed as both orthorhombic/tetragonal and monoclinic phases were excluded from the count. As evident in the histogram, the monoclinic phase dominates in the PDA region (a 72% monoclinic phase composition), while the orthorhombic/tetragonal phases prevail in the PMA region (a 96% orthorhombic/tetragonal phase composition). The relative phase fractions estimated

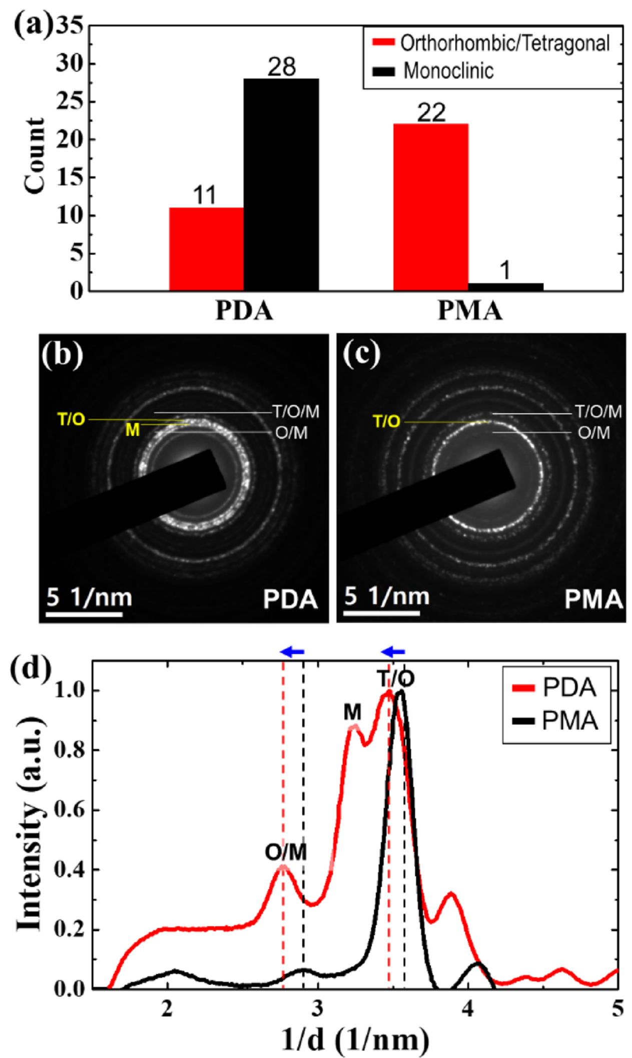

Fig. 3 Phase distribution of HZO thin films after PDA and PMA. **a** Histogram displaying the phase indexing results of HZO thin films in relation to the presence of a TiN TE during annealing. **b**, **c** Selected area electron diffraction (SAED) patterns for HZO thin films after **b** PDA and **c** PMA. **d** Radial intensity profile obtained from SAED patterns shown in (**b**) and (**c**). The letters T, O, and M indicated in the figure represent the tetragonal, orthorhombic, and monoclinic phases, respectively

from HR-TEM analysis are consistent with the higher $2P_r$ of PMA samples than that of PDA samples in Fig. 2. This aligns with previous findings regarding the beneficial role of TiN TE in inducing the orthorhombic phase in HfO_2-based thin films [1, 13, 20]. In Fig. 3b and c, SAED patterns with clear distinctions in the presence of unique peaks corresponding to the monoclinic phase at 3.25 nm^{-1} are displayed. These differences are evident in the radial intensity profile of the SAED pattern presented in Fig. 3d, with the absence of peaks at 3.25 nm^{-1} being noticeable for the PMA region.

3.4 Tensile Stress Effect by TiN Top Electrodes

Notably, there is a slight disparity in the positions of corresponding peaks between the two regions, as indicated in Fig. 3d. In the case of the PDA region, the peaks appear at slightly lower values in the reciprocal space, suggesting larger cell parameters for HZO phases developed without the TiN TE. The lattice parameters calculated from the SAED patterns (Fig. 3b–d) are presented in Fig. 4. It is worth mentioning that the calculated lattice parameter values may not be absolutely precise due to the limited peak intensity and resolution of the SAED patterns. Nevertheless, they are adequate for comparing the difference in lattice parameters between two regions using the same criteria. Additionally, it should be noted that the cell parameters for the monoclinic phase in the PMA region could not be determined due to the insufficient peaks available for the calculation. Further details regarding lattice parameter calculations can be found in the experimental section. Figure 4 demonstrates the larger lattice parameters and volumes for both the orthorhombic and tetragonal phases in the PDA region. Earlier studies have suggested that the primary factor of TiN electrodes driving the transformation of tetragonal precursors into the polar orthorhombic phase in HfO_2-based thin films is the tensile stress/strain induced by the TiN TE during the cooling process [19–21, 23]. However, the larger lattice parameters and volumes observed in the PDA region imply that orthorhombic/tetragonal phases experience higher tensile strain in the absence of the TiN TE, possibly due to the influence of neighboring monoclinic grains. This suggests that the tensile stress/strain originating from the TiN capping layer might not be the most critical factor in the formation of the polar orthorhombic phase.

3.5 Impact on Oxygen Vacancies by TiN Top Electrodes

We also explored the impact of the TiN TE on the oxygen vacancy concentrations in HZO thin films. It is well known that an oxygen-deficient environment can be established in HZO thin films during PMA under a TiN TE, which is believed to hinder the growth of tetragonal precursors, favoring the formation of the orthorhombic phase over the monoclinic phase [10, 12, 13, 24]. To investigate this effect, we performed electron energy loss spectroscopy (EELS) measurements in both the PDA and PMA regions of HZO thin films, as shown in Fig. 5, and compared the results with simulated spectra. To simplify the EELS simulation, HfO_2 structure was employed instead of $Hf_{0.65}Zr_{0.35}O_2$. Given the structural similarity between HfO_2 and $Hf_{0.65}Zr_{0.35}O_2$, it is anticipated to be reasonably valid for comparing the overall trend of EEL spectra changes with respect to the phase of HZO. In Fig. 5a, we present the experimental EEL spectra of the oxygen K-edge. These EEL spectra were obtained by combining data acquired from a sufficiently large area of 0.0625 μm^2 (250 nm × 250 nm), providing an average spectrum of grains in each region. While the positions of peaks are almost similar between the two regions, there is a significant difference in the ratio of the first (A) and the second (B) peaks. HZO after PMA exhibits an A/B ratio of 0.72, while HZO after PDA has a ratio of 0.52. This finding cannot be explained solely by the difference in the phase distribution. Considering the phase distribution from Fig. 3a, where the PDA region is primarily composed of monoclinic phase grains, a higher A/B ratio is expected for the PDA region, as the monoclinic phase exhibits a more intense first peak in the simulated spectrum (Fig. 5d). However, the experimental EEL spectra reveal the opposite result.

This discrepancy can be attributed to differences in the presence of oxygen vacancies in HZO thin films. Our simulated EELS data clearly demonstrates a decrease in the intensity of the first peak in all phases when they contain

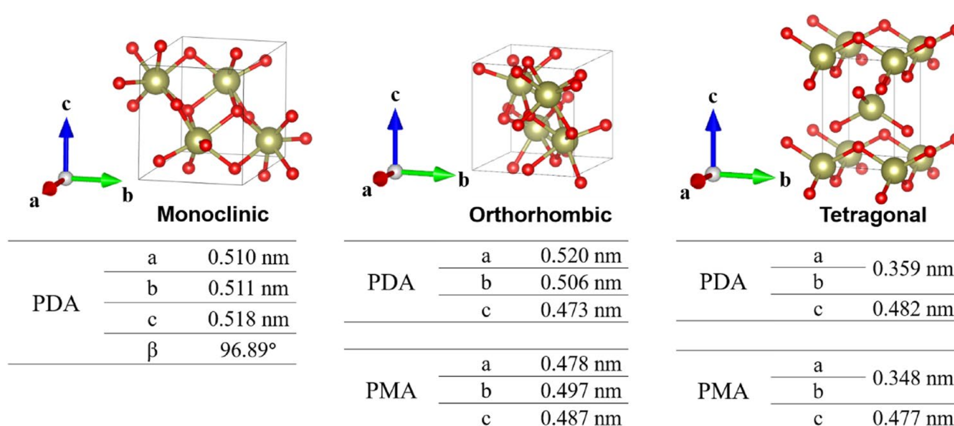

Monoclinic

PDA	a	0.510 nm
	b	0.511 nm
	c	0.518 nm
	β	96.89°

Orthorhombic

PDA	a	0.520 nm
	b	0.506 nm
	c	0.473 nm
PMA	a	0.478 nm
	b	0.497 nm
	c	0.487 nm

Tetragonal

PDA	a, b	0.359 nm
	c	0.482 nm
PMA	a, b	0.348 nm
	c	0.477 nm

Fig. 4 Atomic models and lattice constants of the HZO phases. Lattice constants were determined from the distinct peaks in the SAED patterns presented in Fig. 3b and c. The half-sized cell, containing two Hf atoms and four oxygen atoms in a unit cell, was used for the tetragonal phase

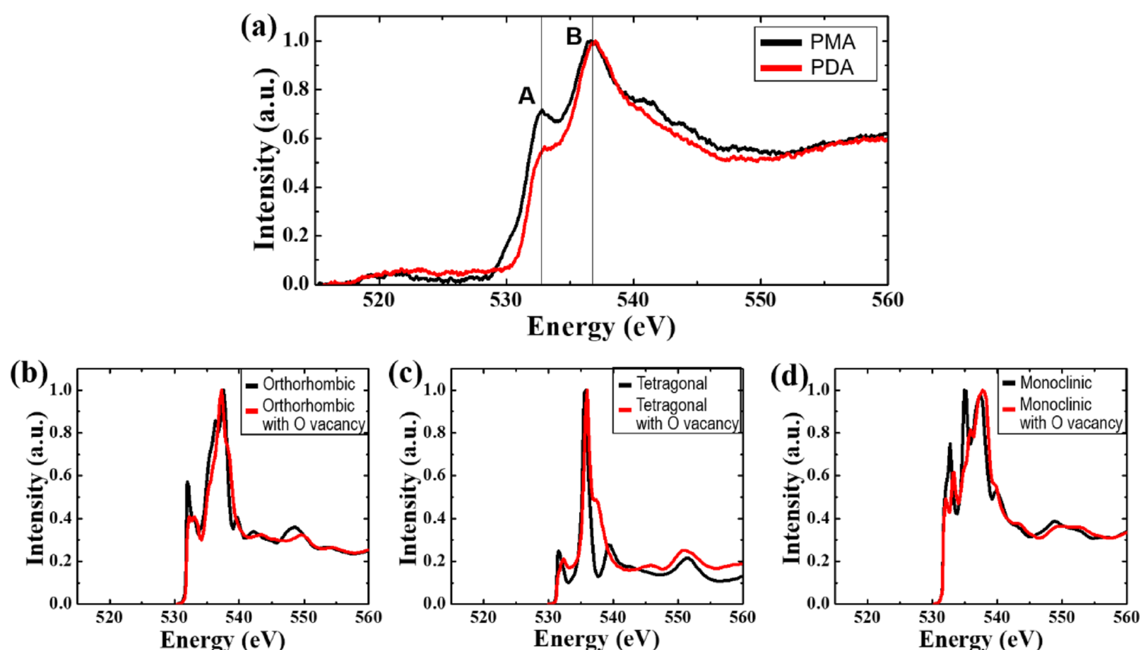

Fig. 5 Electron energy loss (EEL) spectra: **a** Experimental EEL spectra acquired from HZO thin films after PDA and PMA. **b**–**d** Simulated EEL spectra for **b** orthorhombic, **c** tetragonal, and **d** monoclinic phases of HfO_2 with and without oxygen vacancies. The EELS simulation was performed using the FEFF9 code [28, 29]

oxygen vacancies. The reduction of the first peak in the presence of high oxygen vacancy concentrations has also been experimentally confirmed by previous studies [25–27]. Interestingly, our experimental EEL spectra indicate a higher concentration of oxygen vacancies in the PDA region. While the TiN TE does create an oxygen-deficient environment compared to other oxygen-rich electrodes, it appears that significant oxygen loss occurs through the large surface area of the thin film during PDA when no capping layer is present. This suggests that there may be another critical factor related to the TiN TE that significantly contributes to the formation of the polar orthorhombic phase, aside from the influence of an oxygen-deficient environment.

3.6 Surface Atomic Mobility Constraint Effect of TiN Top Electrodes

Grain sizes were further compared using TEM images, with more than 60 grains examined in each region. As shown in Fig. 6, there is a noticeable difference in grain size between the two regions. The grains that grew through the PDA are approximately 70% larger than those that developed through the PMA. This suggests that the TiN TE acted to inhibit grain growth. All of the aforementioned factors, including tensile strain, oxygen vacancies, and the surface atomic mobility constraint effect, have the potential to impede grain growth in HZO thin films. However, it is worth noting that the tensile strain and oxygen vacancy concentrations were found to be even higher in the PDA region (as shown in Figs. 3 and 5), and yet the average grain size is larger than in the PMA region. Therefore, it becomes evident that the surface atomic mobility constraint played a significant role in suppressing grain growth when compared to other factors. It appears that the TiN TE mechanically restricted the mobility of HZO atoms, leading to constraints on grain growth and lattice distortion. This, in turn, suppressed the transformation of tetragonal precursors into the monoclinic phase, which typically has a larger grain size and a distorted cell from the tetragonal phase. This finding aligns well with our phase indexing results presented in Fig. 3 and corroborates with findings from previous studies [1, 30]. Therefore, our comprehensive TEM investigation results suggest that the surface atomic mobility constraint effect of TiN electrodes significantly influences the formation of the polar orthorhombic phase in HZO thin films during the annealing process, thereby enhancing their ferroelectric properties.

4 Conclusion

In our innovative TEM-based research, we uncovered the pivotal role of TiN electrodes in shaping ferroelectric $Hf_{0.65}Zr_{0.35}O_2$ thin films during the annealing process, signifying a transformative development in semiconductor technology. Our unique approach ensured consistent TEM investigation conditions, facilitating a direct structural comparison between HZO films annealed with or without

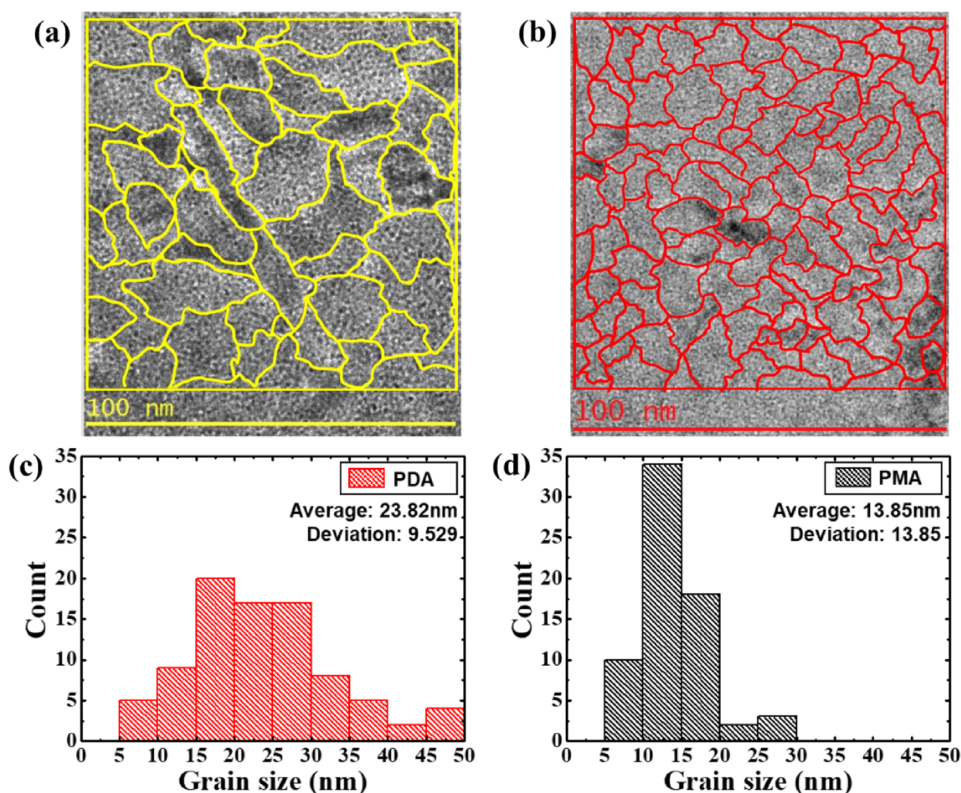

Fig. 6 The grain boundary map of HZO thin films after **a** PDA and **b** PMA, determined from high-resolution TEM images. Histogram depicting grain size distribution of HZO thin films after **c** PDA and **d** PMA, determined from TEM images

a TiN capping layer. Through a comprehensive analysis, encompassing electron diffraction, HR-TEM, and EELS, we identified that the inhibitory effect of TiN electrodes on grain growth by surface atomic mobility constraint significantly drives the formation of the polar orthorhombic phase in HZO thin films, surpassing other potential influences like oxygen vacancies and tensile strain. This breakthrough contributes to the understanding of ferroelectric materials and holds promise for pioneering applications in electronics.

Acknowledgements This work was supported by the National Research Foundation of Korea (NRF) grant funded by the Korean government (MSIT) (No. RS-2023-00222411 and NRF-2022R1C1C1010157). STEM-EELS experiments were conducted using the Spectra 300 TEM instrument at the Korea Research Institute of Standards and Science (KRISS).

Funding This study was funded by Ministry of Science and ICT, South Korea, RS-2023-00222411, Seung-Yong Lee, NRF-2022R1C1C1010157, Seung-Yong Lee.

Data availability The datasets from this study are available from the corresponding author upon reasonable request.

Declaration

Conflict of Interest The authors declare no conflict of interest.

References

1. T.S. Boescke, J. Müller, D. Bräuhaus, U. Schröder, U. Böttger, Appl. Phys. Lett. **99**(10), 102903 (2011). https://doi.org/10.1063/1.3634052
2. U. Schroeder, M.H. Park, T. Mikolajick, C.S. Hwang, Nat. Rev. Mater. **7**(8), 653–669 (2022). https://doi.org/10.1038/s41578-022-00431-2
3. M.H. Park, Y.H. Lee, T. Mikolajick, U. Schroeder, C.S. Hwang, Mrs Commun **8**(3), 795–808 (2018). https://doi.org/10.1557/mrc.2018.175
4. T.D. Huan, V. Sharma, G.A. Rossetti, R. Ramprasad, Phys. Rev. B **90**(6), 064111 (2014). https://doi.org/10.1103/PhysRevB.90.064111
5. S.K. Lee, C.W. Bark, J. Korean Ceram. Soc. **59**(1), 25–43 (2022). https://doi.org/10.1007/s43207-021-00171-z
6. A. Kumar, P. Kumar, A. Dhaliwal, J. Korean Ceram. Soc. **59**(3), 370–382 (2022). https://doi.org/10.1007/s43207-021-00183-9
7. R. Materlik, C. Künneth, M. Falkowski, T. Mikolajick, A. Kersch, J. Appl. Phys. **123**(16), 164101 (2018). https://doi.org/10.1063/1.5021746
8. Z.H. Li, J.C. Wei, J.L. Meng, Y.K. Liu, J.J. Yu, T.Y. Wang, K.L. Xu, P. Liu, H. Zhu, S.Y. Chen, Q.Q. Sun, D.W. Zhang, L. Chen, Nano Lett. **23**(10), 4675–4682 (2023). https://doi.org/10.1021/acs.nanolett.3c00085
9. Y. Ahn, J.Y. Son, J. Korean Ceram. Soc. **60**(2), 301–309 (2023). https://doi.org/10.1007/s43207-022-00265-2
10. Y. H. Lee, H. J. Kim, T. Moon, K. Do Kim, S. D. Hyun, H. W. Park, Y. B. Lee, M. H. Park, C. S. Hwang, Nanotechnology, **28**, 30, 305703 (2017). Doi: https://doi.org/10.1088/1361-6528/aa7624

11. M. Materano, P.D. Lomenzo, A. Kersch, M.H. Park, T. Mikolajick, U. Schroeder, Inorg Chem Front **8**(10), 2650–2672 (2021). https://doi.org/10.1039/d1qi00167a
12. T. Mittmann, T. Szyjka, H. Alex, M.C. Istrate, P.D. Lomenzo, L. Baumgarten, M. Müller, J.L. Jones, L. Pintilie, T. Mikolajick, U. Schroeder, Phys. Status Solidi-R **15**(5), 2100012 (2021). https://doi.org/10.1002/pssr.202100012
13. W. Hamouda, A. Pancotti, C. Lubin, L. Tortech, C. Richter, T. Mikolajick, U. Schroeder, N. Barrett, J. Appl. Phys. **127**(6), 064105 (2020). https://doi.org/10.1063/1.5128502
14. R. Materlik, C. Künneth, A. Kersch, J. Appl. Phys. **117**(13), 134109 (2015). https://doi.org/10.1063/1.4916707
15. P. Polakowski, J. Müller, Appl. Phys. Lett. **106**(23), 232905 (2015). https://doi.org/10.1063/1.4922272
16. M. H. Park, Y. H. Lee, H. J. Kim, Y. J. Kim, T. Moon, K. Do Kim, S. D. Hyun, T. Mikolajick, U. Schroeder, C. S. Hwang, Nanoscale*,* **10**, 2, 716–725 (2018). Doi: https://doi.org/10.1039/c7nr06342c
17. S.S. Cheema, D. Kwon, N. Shanker, R. dos Reis, S.-L. Hsu, J. Xiao, H. Zhang, R. Wagner, A. Datar, M.R. McCarter, C.R. Serrao, A.K. Yadav, G. Karbasian, C.-H. Hsu, A.J. Tan, L.-C. Wang, V. Thakare, X. Zhang, A. Mehta, E. Karapetrova, R.V. Chopdekar, P. Shafer, E. Arenholz, C. Hu, R. Proksch, R. Ramesh, J. Ciston, S. Salahuddin, Nature **580**(7804), 478–482 (2020). https://doi.org/10.1038/s41586-020-2208-x
18. B. Ku, S. Choi, Y. Song, C. Choi, S. Vlsi Tech. (2020). https://doi.org/10.1109/vlsitechnology18217.2020.9265024
19. E.H. Kisi, C.J. Howard, R.J. Hill, J. Am. Ceram. Soc. **72**(9), 1757–1760 (1989). https://doi.org/10.1111/j.1151-2916.1989.tb06322.x
20. S.J. Kim, D. Narayan, J.G. Lee, J. Mohan, J.S. Lee, J. Lee, H.S. Kim, Y.C. Byun, A.T. Lucero, C.D. Young, S.R. Summerfelt, T. San, L. Colombo, J. Kim, Appl. Phys. Lett. **111**(24), 242901 (2017). https://doi.org/10.1063/1.4995619
21. T. Shiraishi, K. Katayama, T. Yokouchi, T. Shimizu, T. Oikawa, O. Sakata, H. Uchida, Y. Imai, T. Kiguchi, T.J. Konno, H. Funakubo, Appl. Phys. Lett. **108**(26), 262904 (2016). https://doi.org/10.1063/1.4954942
22. Y. M. Kim, J. H. Mun, S.-J. Kim, J. Korean Ceram. Soc., 1–13 (2022). Doi: https://doi.org/10.1007/s43207-021-00150-4
23. S. Liu, B.M. Hanrahan, Phys. Rev. Mater. **3**(5), 054404 (2019). https://doi.org/10.1103/PhysRevMaterials.3.054404
24. P. Nukala, M. Ahmadi, Y.F. Wei, S. de Graaf, E. Stylianidis, T. Chakrabortty, S. Matzen, H.W. Zandbergen, A. Björling, D. Mannix, D. Carbone, B. Kooi, B. Noheda, Science **372**(6542), 630–635 (2021). https://doi.org/10.1126/science.abf3789
25. J.H. Jang, H.S. Jung, J.H. Kim, S.Y. Lee, C.S. Hwang, M. Kim, J. Appl. Phys. **109**(2), 023718 (2011). https://doi.org/10.1063/1.3544039
26. G.D. Wilk, D.A. Muller, Appl. Phys. Lett. **83**(19), 3984–3986 (2003). https://doi.org/10.1063/1.1626019
27. S. Kang, W.-S. Jang, A.N. Morozovska, O. Kwon, Y. Jin, Y.-H. Kim, H. Bae, C. Wang, S.-H. Yang, A. Belianinov, Science **376**(6594), 731–738 (2022). https://doi.org/10.1126/science.abk3195
28. M.S. Moreno, K. Jorissen, J.J. Rehr, Micron **38**(1), 1–11 (2007). https://doi.org/10.1016/j.micron.2006.03.011
29. J. Rehr, J. Kas, K. Jorissen, Microsc. Microanal. **22**(S3), 1408–1409 (2016). https://doi.org/10.1017/S1431927616007881
30. X.H. Xu, F.T. Huang, Y.B. Qi, S. Singh, K.M. Rabe, D. Obeysekera, J.J. Yang, M.W. Chu, S.W. Cheong, Nat. Mater. **20**(6), 826 (2021). https://doi.org/10.1038/s41563-020-00897-x

Springer Nature or its licensor (e.g. a society or other partner) holds exclusive rights to this article under a publishing agreement with the author(s) or other rightsholder(s); author self-archiving of the accepted manuscript version of this article is solely governed by the terms of such publishing agreement and applicable law.